Article

A bright millisecond-duration radio burst from a Galactic magnetar

https://doi.org/10.1038/s41586-020-2863-y

Received: 19 May 2020

Accepted: 1 September 2020

Published online: 4 November 2020

Check for updates

The CHIME/FRB Collaboration*

Magnetars are highly magnetized young neutron stars that occasionally produce enormous bursts and flares of X-rays and γ-rays[1]. Of the approximately thirty magnetars currently known in our Galaxy and the Magellanic Clouds, five have exhibited transient radio pulsations[2,3]. Fast radio bursts (FRBs) are millisecond-duration bursts of radio waves arriving from cosmological distances[4], some of which have been seen to repeat[5–8]. A leading model for repeating FRBs is that they are extragalactic magnetars, powered by their intense magnetic fields[9–11]. However, a challenge to this model is that FRBs must have radio luminosities many orders of magnitude larger than those seen from known Galactic magnetars. Here we report the detection of an extremely intense radio burst from the Galactic magnetar SGR 1935+2154 using the Canadian Hydrogen Intensity Mapping Experiment (CHIME) FRB project. The fluence of this two-component bright radio burst and the estimated distance to SGR 1935+2154 together imply a burst energy at 400 to 800 megahertz of approximately 3×10^{34} erg, which is three orders of magnitude higher than the burst energy of any radio-emitting magnetar detected thus far. Such a burst coming from a nearby galaxy (at a distance of less than approximately 12 megaparsecs) would be indistinguishable from a typical FRB. However, given the large gaps in observed energies and activity between the brightest and most active FRB sources and what is observed for SGR 1935+2154-like magnetars, more energetic and active sources—perhaps younger magnetars—are needed to explain all observations.

The CHIME radio telescope at the Dominion Radio Astrophysical Observatory in Penticton, British Columbia consists of four fixed reflecting cylinders, each 20 m × 100 m, oriented north–south, with 256 equispaced antennas sensitive to 400–800-MHz radiation. CHIME is a transit instrument with an instantaneous field of view of approximately 3° × 120°. Digitized and amplified antenna signals are sent to a powerful correlator that provides 1,024 independent sky beams spanning the CHIME field of view; these are searched for FRBs in real time[12].

On 28 April 2020 (all dates and times in UTC unless otherwise indicated), the CHIME/FRB instrument detected a dispersed radio burst during a period of unusually intense X-ray burst activity[13] from the known Galactic magnetar SGR 1935+2154[14]. The burst was detected simultaneously in 93 of the 1,024 CHIME/FRB formed beams, indicating an extremely bright event. The detected event (Fig. 1) consisted of two sub-bursts with best-fit temporal widths of 0.585 ± 0.014 ms and 0.335 ± 0.007 ms (after correcting for propagation and beam-attenuation effects) separated by 28.91 ± 0.02 ms (throughout, all errors represent a 68.3% confidence interval unless otherwise stated). The best-fit estimates of the burst properties are shown in Table 1 (see Methods for a description of the fitting procedure). Both components show clear evidence of multi-path scattering, with a thin-screen scattering timescale of 0.759 ± 0.008 ms (referenced to 600 MHz, with a single scattering function fitted to both burst components).

The detected 'comb-like' spectral structure, as seen in Fig. 1, is characteristic of a CHIME far-sidelobe event, well outside the approximately 3°-wide overhead main lobe of the telescope's primary beam. Using an algorithm that combines the differing detected spectra from the many beams, we reconstructed the burst's sky position to be RA_{J2000} = 19 h 36 min, dec. = +22.1° 6′, with systematic uncertainties of the order of 1° (see Methods), which is 0.3° from the known position of SGR 1935+2154[14], and 22° west of the CHIME meridian. This and the known ongoing intense activity from this magnetar[13] identify the origin of the burst to be SGR 1935+2154.

The two burst components, fitted jointly, have a dispersion measure (DM) of 332.7206 ± 0.0009 pc cm^{-3}, determined from our best-fit spectro-temporal model (Table 1). The maximum DM predicted from the Milky Way along this line of sight is 500–700 pc cm^{-3}, depending on the assumed Galactic electron-density distribution model[15,16]. The source of the burst is thus clearly within our Galaxy, consistent with an association with SGR 1935+2154. The measured DM is also consistent with the source's predicted DM of 530 ± 200 pc cm^{-3} based on a relation between the X-ray absorbing column (N_H) and DM[17] and the measured N_H towards SGR 1935+2154[14]. Additionally, the Faraday rotation measure (RM) determined for the associated supernova remnant, G57.2+0.8, suggests[18] a DM of around 290 pc cm^{-3}, albeit with large uncertainty. The measured DM of the burst sits squarely among these various estimates, further supporting the association.

Immediately following the CHIME/FRB detection of SGR 1935+2154, the 10-m radio dish in Algonquin Provincial Park, Ontario, Canada, which is outfitted with a CHIME feed and which continually records

*A list of participants and their affiliations appears at the end of the paper.

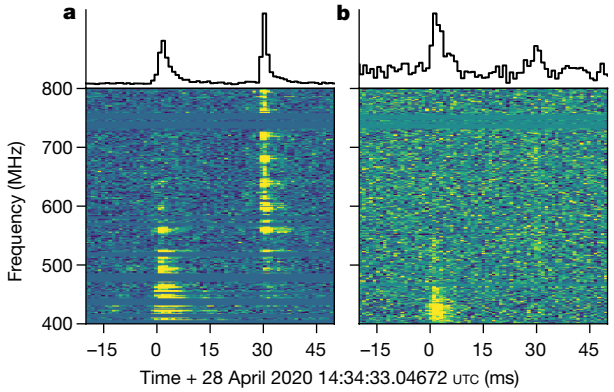

Fig. 1 | Burst waterfalls. a, **b**, Total intensity normalized dynamic spectra and band-averaged time-series (400.1953125-MHz arrival time referenced to the geocentre) of the detections by CHIME/FRB (**a**) and ARO (**b**), relative to the geocentric best-fit arrival time of the first sub-burst based on CHIME/FRB data. For CHIME/FRB, the beam detection with the highest signal-to-noise ratio, *S*/*N*, is shown. Dynamic spectra are displayed at 0.98304-ms and 1.5625-MHz resolution, with intensity values capped at the 1st and 99th percentiles. Frequency channels masked owing to radio-frequency interference are replaced with the median value of the off-burst region. The CHIME/FRB bursts show a 'comb-like' spectral structure owing to their detection in a beam sidelobe as well as dispersed spectral leakage that has an instrumental origin (see Methods).

Table 1 | Properties of the burst from SGR 1935+2154

Parameter	Component 1	Component 2
Dispersion measure (pc cm^{-3})	332.7206(9)	
Scattering timescale (ms)[a]	0.759(8)	
Best-fit *S*/*N*[b]	264	
Arrival time, 28 April 2020 (UTC, topocentric)[c]	14:34:24.40858(2)	14:34:24.43755(2)
Arrival time, 28 April 2020 (UTC, geocentric)[c,d]	14:34:24.42650(2)	14:34:24.45547(2)
Scattering-corrected width (ms)	0.585(14)	0.335(7)
Spectral index[a,b]	−5.75(11)	3.61(8)
Spectral running[b]	1.0(3)	−19.9(3)
Fluence (kJy ms)	480	220
Peak flux density (kJy)	110	150

Values in parentheses denote statistical uncertainties corresponding to the 68.3% confidence interval in the last digit(s).
[a]Quantities are referenced to 600 MHz.
[b]Quantity defined in Methods.
[c]Listed arrival times were corrected for the frequency-dependent time delay from interstellar dispersion using the listed dispersion measure, and are referenced to infinite frequency.
[d]Arrival times at the geocentre were obtained after correcting the listed topocentric times for the geometric delay, assuming an ICRS source position of (RA, dec.) = (19 h 34 min 55.606 s, 21° 53′ 47.4″)[14], and an observatory position of (longitude, latitude, height)$_{CHIME}$ = (119° 36′ 26″ W, 49° 19′ 16″ N, 545 m).

baseband onto a disk buffer, was triggered to save its buffered data. The 10-m dish is presently a testbed for real-time very-long-baseline interferometry of FRBs with CHIME. Analysis of these data (see Methods) provides a measurement of the RM of the event of 116 ± 2 ± 5 rad m^{-2} (measurement and systematic uncertainties, respectively) approximately consistent with previously measured values in this direction[18] as well as with the RM recently reported for a much fainter radio burst detected on 30 April 2020 by the FAST telescope[19]. We find that the position angle of the linear polarization vector of the two burst components is the same to within measurement uncertainties, and set an upper limit on any change of <30° (see Methods).

The occurrence of the burst in a far sidelobe of CHIME, where the sensitivity of the telescope has rapid spatial variation and is not easily calibrated, makes measuring the burst's flux and fluence challenging. Nevertheless, using data from transits of both the Sun and the Crab nebula (which transits 0.12° in declination away from SGR 1935+2154, facilitating comparisons) we have estimated the frequency-dependent sensitivity of CHIME at the location of the detected burst (see Methods). From those measurements, we determine a 400–800-MHz average fluence of 480 kJy ms for the first burst component and 220 kJy ms for the second, for a combined fluence of 700 kJy ms. The band-average peak flux density was 110 kJy for the first component and 150 kJy for the second. All flux density and fluence measurements are subject to a systematic uncertainty of roughly a factor of 2 (see Methods). Our fluence measurement is lower than the 1.5 ± 0.3 MJy ms measured at 1.4 GHz by the Survey for Transient Astronomical Radio Emission 2 (STARE2) instrument[20]. The geocentric arrival time referenced to infinite frequency of the STARE2 detected burst is consistent with our second component. The spectrum of the second component rises steeply towards the top of the 400–800-MHz band and so a higher fluence at 1.4 GHz is not unexpected. The distance to SGR 1935+2154 has been estimated[18,21] to be in the range 6.6–12.5 kpc and we assume a fiducial 10 kpc for what follows. Given our measured peak flux densities and this fiducial distance ($d_{10\,\mathrm{kpc}}$), the 400–800-MHz peak spectral luminosity of the burst is $190^{+190}_{-90}\,d^2_{10\,\mathrm{kpc}}$ MJy kpc, assuming isotropic emission. The burst fluence corresponds to an energy emitted in the 400–800-MHz band of $3^{+3}_{-1.6}\,d^2_{10\,\mathrm{kpc}} \times 10^{34}$ erg and a peak 400–800-MHz luminosity of $7^{+7}_{-4}\,d^2_{10\,\mathrm{kpc}} \times 10^{36}$ erg s^{-1}.

Several high-energy telescopes reported the detection of a two-component hard X-ray/soft γ-ray burst at the time of the radio event from SGR 1935+2154[22–24]. The reported arrival times from the Insight-HXMT (Hard X-ray Modulation Telescope) for the two components of the X-ray burst corrected to the geocentre are 14:34:24.4289 and 14:34:24.4589 UTC[24,25]. The two X-ray components each occurred within about 3 ms of the respective dispersion-corrected geocentric arrival times of the CHIME burst components (see Table 1). The fluence of the soft γ-ray burst in the 20–200-keV band, as reported by the Konus-Wind experiment[23], was 7.63(0.75) × 10^{-7} erg cm^{-2}. Our measured fluence, 700^{+700}_{-350} kJy ms, gives a radio-to-γ-ray fluence ratio of $9^{+9}_{-5} \times 10^{11}$ Jy ms erg^{-1} cm^2 (or $4^{+4}_{-2} \times 10^{-6}$ in dimensionless units factoring in the 400-MHz CHIME bandwidth). This is five orders of magnitude above the upper limit on the ratio based on the non-detection of radio emission[26] at the time of a giant flare from Galactic magnetar SGR 1806–20 and two orders of magnitude above the lower limit placed on the fluence ratio from the non-detection of high-energy emission at the time of radio bursts[27] from the repeating source FRB 121102.

The SGR 1935+2154 radio burst was detected during an extended active phase of the magnetar, in which hundreds of high-energy bursts were reported. We note that four other reported[28–30] soft γ-ray bursts occurred at times when the source was at a similar or smaller hour angle than the detected radio burst from the CHIME meridian, on 4 and 5 November 2019. The two events on 5 November had high-energy fluxes 14 and 11 times smaller, respectively, than that of the 28 April 2020 event (see Methods). Yet, CHIME/FRB detected no radio events at those epochs, with conservative 3σ flux density upper limits in our band of <1.2 kJy and <3.0 kJy, respectively, implying radio-to-high-energy flux ratios at least 9 and 4 times smaller, respectively (see Methods). Radio counterparts to high-energy bursts from magnetars are thus either not emitted at every burst, or extend to low flux ratios. Alternatively, geometric effects such as beaming of the radio emission may hinder radio-burst observability.

The radio burst from SGR 1935+2154 is by far the most radio-luminous such event detected from any Galactic magnetar. Five other Galactic magnetars have been observed to emit radio pulsations[2,3]. These pulsations are made up of short millisecond duration 'spiky' subpulses[3,31], which sometimes show spectral variations[31] reminiscent

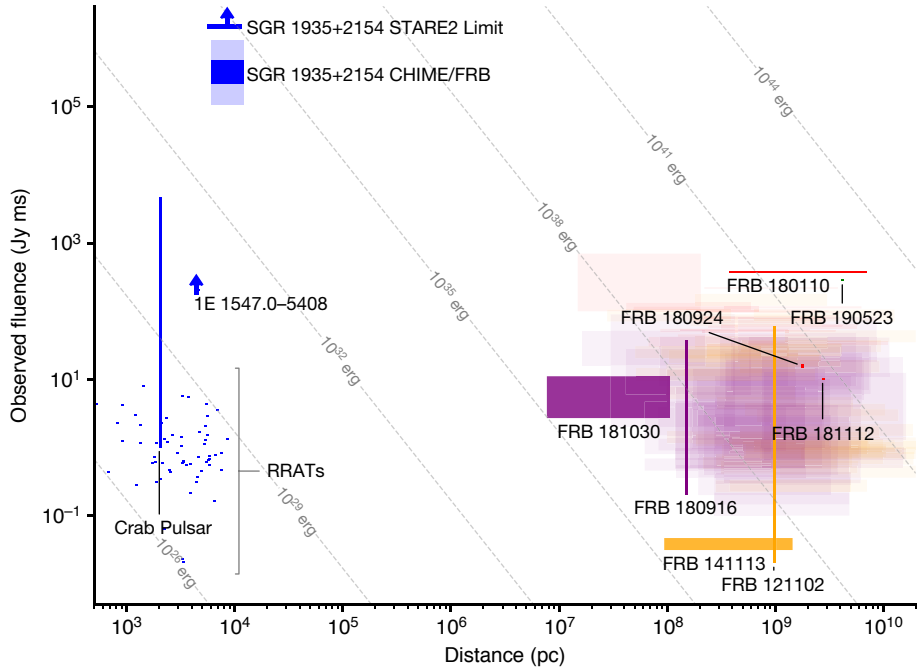

Fig. 2 | Comparison of short radio burst energetics. The observed burst fluences at radio frequencies from 300 MHz to 1.5 GHz for Galactic neutron stars and extragalactic FRBs are plotted with their estimated distances. The fluence ranges include the uncertainties in fluence measurements as well as ranges of individual bursts for repeating FRBs and pulsars. FRBs colours indicate their detection telescope: CHIME/FRB (purple), the Australian Square Kilometre Array Pathfinder (ASKAP; red), the Deep Synoptic Array (DSA-10; green, FRB 190523), Arecibo and Parkes (orange). Galactic sources are plotted in blue. For SGR 1935+2154, the blue rectangle indicates the nominal range of 400–800-MHz fluences measured for the two bursts, and the light-blue region incorporates the possible systematic uncertainty in the CHIME/FRB fluence as described in the text. The STARE2 lower limit on the fluence at 1.4 GHz is also shown. The grey diagonal lines indicate the loci of equal isotropic burst energy with an assumed fiducial bandwidth of 500 MHz. FRB distances are estimated from their extragalactic dispersion-measure contribution including the simulated variance[38]. Pulsar distances are estimated on the basis of the NE2001 Galactic electron-distribution model[15]. Objects with accurately measured distances (parallax or host galaxy redshift) are indicated with vertical lines. RRAT, rotating radio transient.

of those seen in some FRBs[6,8,32]. These, however, have thus far been observed to be many orders of magnitude fainter than the radio burst from SGR 1935+2154. The brightest radio burst previously seen from a magnetar (see Fig. 2) was three orders of magnitude fainter; it had fluence >200 Jy ms at 6 GHz[33] and occurred during the 2009 outburst of magnetar 1E 1547.0–5408 (which showed an X-ray burst 'forest' similar to that[13] of SGR 1935+2154). Giant pulses from the Crab pulsar have been observed up to a fluence[34] of around 5 kJy ms which, at the distance of the Crab nebula, corresponds to an energy of 10^{31} erg (Fig. 2), also about three orders of magnitude less energetic than the radio burst from SGR 1935+2154. Thus, the 28 April event from SGR 1935+2154 clearly signals that magnetars can produce far brighter radio bursts than have been previously observed in our Galaxy.

The SGR 1935+2154 radio burst has implications for magnetars as potential sources of FRBs. In Fig. 2 we show the fluences, distances and implied burst energies from extragalactic FRBs alongside Galactic sources of short-duration radio emission, such as magnetars and pulsars. Here and in Fig. 2, a fiducial emitting bandwidth of 500 MHz is assumed when translating fluences to burst energies. Notably, the bursts from the nearest extragalactic FRB source with a well determined distance, FRB 180916.J0158+65 (observed fluences spanning 0.2 Jy ms[35] to 37 Jy ms[36] and luminosity distance of 149 Mpc[35]), have implied radio energies of 3×10^{36} erg to 4×10^{38} erg. Other FRBs with only DM-estimated distances, such as FRB 181030.J1054+73[6] and FRB 141113[37], are potentially even less energetic, with DM-implied distances that put their energies as low as approximately 10^{35} erg s^{-1}. This places the event from SGR 1935+2154 only 1–2 orders of magnitude below the observed burst energies of typical FRBs, but the SGR 1935+2154 burst could have similar energies to bursts from FRB 181030 and FRB 141113 if they were at their nearest possible distance. As the detection of these faint FRBs is limited by the sensitivity of our instruments, the intrinsic luminosity distribution of the faintest FRB sources may overlap with that of the event from SGR 1935+2154. This detection has therefore substantially narrowed the vast luminosity gap between what had been observed from Galactic sources in the past and what is observed from extragalactic FRBs.

However, FRBs at cosmological distances can be much more energetic. For example, FRB 180110, one of the most energetic FRBs reported so far, is at a luminosity distance of about 3–5 Gpc given its DM excess[38], and was detected with a fluence of approximately 390 Jy ms[39]. This implies an emitted energy of 10^{42}–10^{43} erg. This is 8 to 9 orders of magnitude more energetic than the burst from SGR 1935+2154. It is as yet unclear whether such energetic events could be generated by conventional magnetars, though the total energies are plausibly within the range of magnetar energetics. For example, the most energetic Galactic magnetar giant flare, from SGR 1806–20 in 2004, emitted around 10^{47} erg at γ-ray wavelengths[40]. If we scale using the same radio-to-γ-ray efficiency from the SGR 1935+2154 event, 4×10^{-6}, the implied radio counterpart would have a radio energy of about 10^{41} erg, which is similar to the energies of the brightest FRBs (see Fig. 2).

The morphology of the burst from SGR 1935+2154 resembles those detected from FRBs. The approximately 1-ms measured durations of the subcomponents are typical of the widths of bursts from the 18 repeating FRB sources discovered by CHIME[6,8]. The broad spectra of the two SGR 1935+2154 components are strikingly different between the two components, with the first detected primarily at frequencies under about 600 MHz and the second above this frequency. Although the frequency-dependent telescope response is complicated for this off-axis detection, it does not vary on the timescale of the separation between the two bursts. Extreme burst-to-burst spectral variations are

common in repeating FRBs[5,8]. However, a common feature in repeating FRB morphologies is multiple subcomponents marching downward in frequency[6,8,32]—opposite to what is seen in the 28 April event from SGR 1935+2154, where the two components increase in frequency (see Fig. 1). The 29-ms separation between the two components is larger than is typically observed[6,8], which could signal two distinct events instead of one with drifting. Also, upward frequency drifting in FRBs is not completely unprecedented; for example, one of the bursts from FRB 180916.J0158+65 on MJD 58720 (MJD, modified Julian date) shows two components separated by 60 ms with the second detected at higher frequencies than the first[36].

Models for magnetars as sources of FRBs fall into two main classes. For models in which the radio waves are produced in the magnetosphere of an active magnetar[41,42] the short durations and separation of the two radio bursts are natural, as is the radio-to-γ-ray burst-time separation of less than a few milliseconds. Although a magnetospheric magnetar model might suggest periodicities at the neutron-star rotation rate, the apparent absence thereof[43] in one prolific FRB (121102) could be consistent with the lack of spin–phase dependence of bursts in some magnetars[1]. The other main class of magnetar model involves the neutron star as a central engine in a surrounding nebula of past outflow material, wherein a high-energy flare creates an FRB via a synchrotron maser blast wave at a typically large distance ($r \approx 10^{13} - 10^{15}$ cm) from the magnetar[9–11]. In such models, the high-energy emission from the flare should precede the radio burst by the light travel time to the maser emission region, much longer than the <1-ms coincidence observed for SGR 1935+2154, unless the flow is highly relativistic or the dimensions are greatly scaled down in the SGR 1935+2154 system such that $r/\Gamma \approx 3 \times 10^7$ cm, where Γ is the Lorentz factor. The radio-to-high-energy emission efficiency of approximately 10^{-6} is as predicted in these FRB models. For both models, the absence of radio bursts at all high-energy burst epochs, as reported here and elsewhere[26], could be due to the required relativistic beaming. Downward frequency drifts, as seen in many repeating FRB bursts[6,8,32], are involved in both sets of models but are unseen in this and other Galactic magnetar radio bursts.

It remains to be seen whether the population of FRBs, which has a burst rate[44,45] of approximately 2×10^3–2×10^5 Gpc^{-3} yr^{-1}, can be explained by a single population of SGR 1935+2154-like magnetars. On the basis of the CHIME/FRB detection of the 28 April burst from SGR 1935+2154 and the CHIME/FRB non-detection of bursts from nearby star-forming galaxies, in spite of ample exposure to them (see Methods), we constrain the rate of magnetar bursts with energy $E > 10^{34}$ erg to be 0.007–0.4 yr^{-1} for a typical Galactic magnetar. The rate of bursts at $E > 10^{36}$ erg is constrained to be <0.004 yr^{-1} from the non-detection of FRBs from the Virgo cluster[46] (see Methods), albeit at a different radio frequency.

On the basis of these two constraints, and assuming that the magnetar burst rate follows a power-law distribution with rate $R(>E) \propto E^{\alpha}$, we calculate an upper limit to the rate of magnetar bursts with typical FRB energies ($E \gtrsim 10^{38}$ erg) to be <0.002 yr^{-1} per magnetar, with the power-law index limited to $\alpha \gtrsim -0.15$.

Given the ubiquity of magnetars, which form at around 10–50% of the core-collapse supernova rate[47], or (1–5) × 10^4 Gpc^{-3} yr^{-1}, and have an active lifetime[1] of $\tau \approx 10^3$ yr, magnetars could generate bursts up to a volumetric rate 10^5 Gpc^{-3} yr^{-1}, comparable to that of FRBs. We note that this rate reflects a limiting value of $\alpha \approx -0.15$, much flatter than those inferred for repeat bursts from FRB 121102 ($\alpha = -1.8 \pm 0.3$)[48] or for repeating FRB 180916 ($\alpha = -2.5 \pm 0.4$)[36].

Moreover, SGR 1935+2154-like magnetars are unlikely to explain extremely prolific repeating FRBs such as FRB 121102, which has emitted 18 bursts with energies >10^{37} erg in 30 min[49], or to be found in the outskirts of elliptical galaxies[50]. These observations suggest that extragalactic analogues of current Galactic magnetars could explain some of the FRB population, but much more active—perhaps younger—sources, and/or those with non-core-collapse origins, must still be invoked to explain all existing FRB observations.

Online content

Any methods, additional references, Nature Research reporting summaries, source data, extended data, supplementary information, acknowledgements, peer review information; details of author contributions and competing interests; and statements of data and code availability are available at https://doi.org/10.1038/s41586-020-2863-y.

1. Kaspi, V. M. & Beloborodov, A. M. Magnetars. *Annu. Rev. Astron. Astrophys.* **55**, 261–301 (2017).
2. Olausen, S. A. & Kaspi, V. M. The McGill Magnetar Catalog. Astrophys. *J. Suppl. Ser.* **212**, 6 (2014).
3. Esposito, P. et al. A very young radio-loud magnetar. *Astrophys. J. Lett.* **896**, 30 (2020).
4. Petroff, E., Hessels, J. W. T. & Lorimer, D. R. Fast radio bursts. *Astron. Astrophys. Rev.* **27**, 4 (2019).
5. Spitler, L. G. et al. A repeating fast radio burst. *Nature* **531**, 202–205 (2016).
6. The CHIME/FRB Collaboration. CHIME/FRB detection of eight new repeating fast radio burst sources. *Astrophys. J. Lett.* **885**, 24 (2019).
7. Kumar, P. et al. Faint repetitions from a bright fast radio burst source. *Astrophys. J. Lett.* **887**, 30 (2019).
8. Fonseca, E. et al. Nine new repeating fast radio burst sources from CHIME/FRB. *Astrophys. J. Lett.* **891**, 6 (2020).
9. Lyubarsky, Y. A model for fast extragalactic radio bursts. *Mon. Not. R. Astron. Soc.* **442**, L9–L13 (2014).
10. Beloborodov, A. M. A flaring magnetar in FRB 121102? Astrophys. *J. Lett.* **843**, 26 (2017).
11. Metzger, B. D., Margalit, B. & Sironi, L. Fast radio bursts as synchrotron maser emission from decelerating relativistic blast waves. *Mon. Not. R. Astron. Soc.* **485**, 4091–4106 (2019).
12. CHIME/FRB Collaboration et al. The CHIME Fast Radio Burst Project: system overview. *Astrophys. J.* **863**, 48 (2018).
13. Palmer, D. M. A forest of bursts from SGR 1935+2154. *Astron. Telegr.* 13675 (2020).
14. Israel, G. L. et al. The discovery, monitoring and environment of SGR J1935+2154. *Mon. Not. R. Astron. Soc.* **457**, 3448–3456 (2016).
15. Cordes, J. M. & Lazio, T. J. W. NE2001. I. A new model for the galactic distribution of free electrons and its fluctuations. Preprint at https://arxiv.org/abs/astro-ph/0207156 (2002).
16. Yao, J. M., Manchester, R. N. & Wang, N. A new electron-density model for estimation of pulsar and FRB distances. *Astrophys. J.* **835**, 29 (2017).
17. He, C., Ng, C.-Y. & Kaspi, V. The correlation between dispersion measure and X-ray column density from radio pulsars. *Astrophys. J.* **768**, 64 (2013).
18. Kothes, R., Sun, X., Gaensler, B. & Reich, W. A radio continuum and polarization study of SNR G57.2+0.8 associated with magnetar SGR 1935+2154. *Astrophys. J.* **852**, 54 (2018).
19. Zhang, C. F. et al. A highly polarised radio burst detected from SGR 1935+2154 by FAST. *Astron. Telegr.* 13699 (2020).
20. CHIME/FRB. A fast radio burst associated with a Galactic magnetar. Nature https://doi.org/10.1038/s41586-020-2872-x (2020).
21. Zhou, P. et al. Revisiting the distance, environment and supernova properties of SNR G57.2+0.8 that hosts SGR 1935+2154. Preprint at https://arxiv.org/abs/2005.03517 (2020).
22. Mereghetti, S. et al. INTEGRAL IBIS and SPI-ACS detection of a hard X-ray counterpart of the radio burst from SGR 1935+2154. *Astron. Telegr.* 13685 (2020).
23. Ridnaia, A. et al. Konus-Wind observation of hard X-ray counterpart of the radio burst from SGR 1935+2154. *Astron. Telegr.* 13688 (2020).
24. Zhang, S. N. et al. Insight-HXMT X-ray and hard X-ray detection of the double peaks of the fast radio burst from SGR 1935+2154. *Astron. Telegr.* 13696 (2020).
25. Zhang, S. N. et al. Geocentric time correction for Insight-HXMT detection of the X-ray counterpart of the FRB by CHIME and STARE2 from SGR 1935+2154. *Astron. Telegr.* 13704 (2020).
26. Tendulkar, S. P., Kaspi, V. M. & Patel, C. Radio nondetection of the SGR 1806–20 giant flare and implications for fast radio bursts. *Astrophys. J.* **827**, 59 (2016).
27. Scholz, P. et al. Simultaneous X-ray, gamma-ray, and radio observations of the repeating fast radio burst FRB 121102. *Astrophys. J.* **846**, 80 (2017).
28. von Kienlin, A. Fermi GBM GRBs 191104 A, B, C and triggers 594534420/191104185 and 594563923/191104527 are not GRBs. *GCN Circ.* 26163 (2019).
29. Ambrosi, E., D'Elia, V., Kennea, J. A. & Palmer, D. Trigger 933276: Swift detection of further activity from SGR 1935+2154. *GCN Circ.* 26169 (2019).
30. Palmer, D. Trigger 933285: Swift detection of the brightest burst so far from SGR 1935+2154. *GCN Circ.* 26171 (2019).
31. Pearlman, A. B., Majid, W. A., Prince, T. A., Kocz, J. & Horiuchi, S. Pulse morphology of the Galactic Center magnetar PSR J1745–2900. *Astrophys. J.* **866**, 160 (2018).
32. Hessels, J. W. T. et al. FRB 121102 bursts show complex time–frequency structure. *Astrophys. J. Lett.* **876**, 23 (2019).
33. Burgay, M. et al. Search for FRB and FRB-like single pulses in Parkes magnetar data. In *Pulsar Astrophysics: the Next Fifty Years* (eds Weltevrede, P. et al.) 319–321 (2018).
34. Bera, A. & Chengalur, J. N. Super-giant pulses from the Crab pulsar: energy distribution and occurrence rate. *Mon. Not. R. Astron. Soc.* **490**, L12–L16 (2019).
35. Marcote, B. et al. A repeating fast radio burst source localized to a nearby spiral galaxy. *Nature* **577**, 190–194 (2020).
36. The CHIME/FRB Collaboration. Periodic activity from a fast radio burst source. *Nature* **582**, 351–355 (2020).
37. Patel, C. et al. PALFA single-pulse pipeline: new pulsars, rotating radio transients, and a candidate fast radio burst. *Astrophys. J.* **869**, 181 (2018).
38. Pol, N., Lam, M. T., McLaughlin, M. A., Lazio, T. J. W. & Cordes, J. M. Estimates of fast radio burst dispersion measures from cosmological simulations. *Astrophys. J.* **886**, 135 (2019).

39. Shannon, R. M. et al. The dispersion–brightness relation for fast radio bursts from a wide-field survey. *Nature* **562**, 386–390 (2018).
40. Hurley, K. et al. An exceptionally bright flare from SGR 1806–20 and the origins of short-duration γ-ray bursts. *Nature* **434**, 1098–1103 (2005).
41. Lyutikov, M. Radio emission from magnetars. *Astrophys. J. Lett.* **580**, 65–68 (2002).
42. Kumar, P., Lu, W. & Bhattacharya, M. Fast radio burst source properties and curvature radiation model. *Mon. Not. R. Astron. Soc.* **468**, 2726–2739 (2017).
43. Zhang, Y. G. et al. Fast radio burst 121102 pulse detection and periodicity: a machine learning approach. *Astrophys. J.* **866**, 149 (2018).
44. Bhandari, S. et al. The Survey for Pulsars and Extragalactic Radio Bursts—II. New FRB discoveries and their follow-up. *Mon. Not. R. Astron. Soc.* **475**, 1427–1446 (2018).
45. Ravi, V. The prevalence of repeating fast radio bursts. *Nat. Astron.* **3**, 928–391 (2019).
46. Agarwal, D. et al. A fast radio burst in the direction of the Virgo cluster. *Mon. Not. R. Astron. Soc.* **490**, 1–8 (2019).
47. Taylor, M. et al. The core collapse supernova rate from the SDSS-II Supernova Survey. *Astrophys. J.* **792**, 135 (2014).
48. Gourdji, K. et al. A sample of low-energy bursts from FRB 121102. *Astrophys. J. Lett.* **877**, 19 (2019).
49. Gajjar, V. et al. Highest frequency detection of FRB 121102 at 4–8 GHz using the Breakthrough Listen digital backend at the Green Bank Telescope. *Astrophys. J.* **863**, 2 (2018).
50. Bannister, K. W. et al. A single fast radio burst localized to a massive galaxy at cosmological distance. *Science* **365**, 565–570 (2019).

The CHIME/FRB Collaboration

B. C. Andersen[1,2], K. M. Bandura[3,4], M. Bhardwaj[1,2], A. Bij[5], M. M. Boyce[6], P. J. Boyle[1,2], C. Brar[1,2], T. Cassanelli[7,8], P. Chawla[1,2], T. Chen[9], J.-F. Cliche[1,2], A. Cook[7,8], D. Cubranic[10], A. P. Curtin[1,2], N. T. Denman[11], M. Dobbs[1,2], F. Q. Dong[10], M. Fandino[10], E. Fonseca[1,2], B. M. Gaensler[7,8], U. Giri[12,13], D. C. Good[10], M. Halpern[10], A. S. Hill[14,15], G. F. Hinshaw[10], C. Höfer[10], A. Josephy[1,2], J. W. Kania[16], V. M. Kaspi[1,2], T. L. Landecker[15], C. Leung[9,17], D. Z. Li[5,7,18,19], H.-H. Lin[5,19], K. W. Masui[9,17], R. Mckinven[7,8], J. Mena-Parra[9], M. Merryfield[1,2], B. W. Meyers[10], D. Michilli[1,2], N. Milutinovic[10], A. Mirhosseini[10], M. Münchmeyer[12], A. Naidu[1,2], L. B. Newburgh[20], C. Ng[7], C. Patel[1,7], U.-L. Pen[5,7,12,19,21], T. Pinsonneault-Marotte[10], Z. Pleunis[1,2], B. M. Quine[22,23], M. Rafiei-Ravandi[12], M. Rahman[7], S. M. Ransom[24], A. Renard[7], P. Sanghavi[3,4], P. Scholz[7]✉, J. R. Shaw[10], K. Shin[9,17], S. R. Siegel[1,2], S. Singh[1,2], R. J. Smegal[10], K. M. Smith[12], I. H. Stairs[10], C. M. Tan[1,2], S. P. Tendulkar[1,2], I. Tretyakov[7,18], K. Vanderlinde[7,8], H. Wang[9], D. Wulf[1,2] & A. V. Zwaniga[1,2]

[1]Department of Physics, McGill University, Montreal, Quebec, Canada. [2]McGill Space Institute, McGill University, Montreal, Quebec, Canada. [3]CSEE, West Virginia University, Morgantown, WV, USA. [4]Center for Gravitational Waves and Cosmology, West Virginia University, Morgantown, WV, USA. [5]Canadian Institute for Theoretical Astrophysics, Toronto, Ontario, Canada. [6]Department of Physics and Astronomy, University of Manitoba, Winnipeg, Manitoba, Canada. [7]Dunlap Institute for Astronomy and Astrophysics, University of Toronto, Toronto, Ontario, Canada. [8]David A. Dunlap Department of Astronomy and Astrophysics, University of Toronto, Toronto, Ontario, Canada. [9]MIT Kavli Institute for Astrophysics and Space Research, Massachusetts Institute of Technology, Cambridge, MA, USA. [10]Department of Physics and Astronomy, University of British Columbia, Vancouver, British Columbia, Canada. [11]Central Development Laboratory, National Radio Astronomy Observatory, Charlottesville, VA, USA. [12]Perimeter Institute for Theoretical Physics, Waterloo, Ontario, Canada. [13]Department of Physics and Astronomy, University of Waterloo, Waterloo, Ontario, Canada. [14]Department of Computer Science, Math, Physics, and Statistics, University of British Columbia, Kelowna, British Columbia, Canada. [15]Herzberg Research Centre for Astronomy and Astrophysics, Dominion Radio Astrophysical Observatory, National Research Council Canada, Penticton, British Columbia, Canada. [16]Department of Physics and Astronomy, West Virginia University, Morgantown, WV, USA. [17]Department of Physics, Massachusetts Institute of Technology, Cambridge, MA, USA. [18]Department of Physics, University of Toronto, Toronto, Ontario, Canada. [19]Max-Planck-Institut für Radioastronomie, Bonn, Germany. [20]Department of Physics, Yale University, New Haven, CT, USA. [21]CIFAR Program in Gravitation and Cosmology, Canadian Institute for Advanced Research, Toronto, Ontario, Canada. [22]Algonquin Radio Observatory, Thoth Technology, Pembroke, Ontario, Canada. [23]Department of Physics and Astronomy, York University, Toronto, Ontario, Canada. [24]National Radio Astronomy Observatory, Charlottesville, VA, USA. ✉e-mail: paul.scholz@dunlap.utoronto.ca

Methods

Localization

To determine the sky location of the event, we fitted a model for the CHIME/FRB synthesized beam[51,52] and underlying Gaussian burst spectrum to the measured spectra of the brighter second burst component. The free parameters in the model were the sky position and the width, mean and amplitude of the Gaussian spectral model. Sixty-eight burst spectra were fitted: 54 from the main cluster of beams that detected the event (out of a total of 93 detection beams) plus 14 from the adjacent non-detection beams. The fitting was performed using a Markov chain Monte Carlo method[53] with a flat prior on the position of the event in a 108° (E–W) × 10° (N–S) region centred on the CHIME meridian at the zenith angle of the beam with the brightest detection. In this large area of the sky searched, the localization optimization settled on a position of RA = 19 h 35 min 35.9 s, dec. = 22.1°, which is 0.3° from the position of SGR 1935+2154. As this localization method is still in development, and is largely untested for events this far off the CHIME meridian, we believe there are large as-yet-unquantified systematic uncertainties of the order of 1° and so do not report the statistical uncertainties on the fit, which are subdominant.

Estimate of burst fluence

The central challenge of obtaining a flux calibration for the burst is characterizing the primary-beam response far outside its main lobe, where the telescope was optimized for detection and calibration. The CHIME primary-beam main lobe covers a narrow strip along the meridian centred at hour angle (HA) = 0 and 2°–3° wide depending on frequency, and extends about ±60° in elevation. When the burst was detected, SGR 1935+2154 was at HA = 22°. We measure the primary-beam response at this location using both interferometric measurements of the sun and holographic measurements of the Crab nebula. Although both measurements are fundamentally interferometric in nature, they are subject to different systematics—not least of which is the use of different celestial sources (that is, the Sun versus the Crab nebula). As will be explained in more detail below, the two measurements are made using different antenna-baseline configurations, and use fairly independent gain-normalization schemes.

The proximity in declination of the Crab nebula to SGR 1935+2154 provides a fortuitous means of calibrating the primary beam at that declination as a function of hour angle. The Crab nebula is located roughly 0.12° north in declination from the SGR 1935+2154, which induces a systematic error of the order of 10% (estimated from the solar data described below). Because SGR 1935+2154 is located HA = 22° from meridian, far into the sidelobes of the primary beam, interferometric data from the CHIME telescope alone contains too much confusion noise from other radio sources to estimate the beam using the Crab nebula. To eliminate confusion with other sources, and to boost the signal in this low-sensitivity part of the beam, we employ a version of the standard radio holographic technique. We track the Crab nebula using the co-located Dominion Radio Astrophysical Observatory (DRAO) 26-m Galt telescope, outfitted with a 400–800-MHz receiver, and perform interferometry with the stationary CHIME antennas[54,55]. The resulting data provide a measurement of the complex response of each antenna and polarization in the CHIME array along the source transit path in hour angle, which contains only correlated power between the primary CHIME telescope beam and the primary Galt telescope beam. In traditional radio holography, such a measurement would then be transformed to make a map of the aperture of the telescope, usually to assess telescope surface.

The quantity we wish to measure is the complex beam response to an unpolarized source, averaged over the array of feeds and summed in intensity over polarization channels. Following a previous formalism[52], we write this as:

$$B(\theta) \equiv \frac{1}{n_{\mathrm{ant}}} \sum_{p} \left| \sum_{i} \mathbf{A}_{ip}(\theta) \right|^2, \quad (1)$$

where $\mathbf{A}_{ip}(\theta)$ is the direction-dependent response to the vector electric field of feed i and polarization channel p, and n_{ant} is the number of feeds. Here we have suppressed the spectral frequency axis, and the beam measurement should be understood to be performed independently in each spectral channel. In this case, we have made a measurement at a single declination and thus θ is simply the hour angle during the transit of the Crab nebula. The measured holographic visibility can be used to estimate $\mathbf{A}_{ip}(\theta)$ for CHIME, and is defined as:

$$V^{\mathrm{meas}}_{ip,p'}(\theta) = g^{\mathrm{C}}_{ip} g^{\mathrm{Galt}}_{p'} \boldsymbol{\epsilon}_{p'} \cdot \mathbf{A}_{ip}(\theta) S_{\nu}, \quad (2)$$

where $g^{\mathrm{Galt}}_{p'}$ is the overall gain of the polarization channel p' of the Galt Telescope (including optical, analogue, and digital contributions), $\boldsymbol{\epsilon}_{p'}$ is the unit vector denoting the direction of the channel's polarization response (we assume these to be orthogonal for the two Galt polarization channels), g^{C}_{ip} is a per-feed gain factor for the CHIME telescope (analogue and digital contributions), set to a real number by phase-referencing at the Crab nebula transit, and S_{ν} is the frequency-dependent source flux density of the Crab nebula in Jy.

To use the holographic visibilities as an estimate of the CHIME beam, we must account for a few scalings.

First, the holographic visibility for a given CHIME polarization channel, p, is normalized by the total power measured on meridian. This term is the sum of the powers in the co-polarization and cross-polarization between CHIME and the Galt telescope:

$$\sqrt{\textstyle\sum_{p'} |V_{ip,p'}(0)|^2}\,.$$

Second, the gains between the two polarization channels on the Galt telescope are not equal. We can calibrate the relative gains between the two polarizations using the Galt autocorrelations:

$$V^{\mathrm{Galt}}_{p,p} \propto \left| g^{\mathrm{Galt}}_{p} \right|^2 S_{\nu}. \quad (3)$$

We have neglected the contribution from the receiver temperature, owing to the brightness of the Crab nebula and the high gain of the Galt telescope. Dividing by the square root of the autocorrelations removes the dependence on the relative gains of the two polarizations. This modifies the normalization factor derived from the total power above, as:

$$\sqrt{V_{p',p'} \textstyle\sum_{p''} (|V_{ip,p''}(0)|^2 / V_{p'',p''})}\,.$$

Third, the gain for each CHIME feed on meridian is computed and stored for bright transits, including the Crab nebula. We can use this to scale the holographic data, per feed and polarization, to the CHIME response values at meridian: $\mathbf{A}_{ip}(0)$, which also accounts for the g^{C}_{ip} term in equation (2).

Provided that the direction of $\mathbf{A}_{ip}(0)$ does not depend on i (which is empirically true at the 1% level), the desired beam response can then be written as:

$$B(\theta) = \frac{1}{n_{\mathrm{ant}}} \sum_{p,p'} \left| \sum_{i} \frac{V_{ip,p'}(\theta) \mathbf{A}_{ip}(0)}{\sqrt{V_{p',p'} \textstyle\sum_{p''} (|V_{ip,p''}(0)|^2 / V_{p'',p''})}} \right|^2. \quad (4)$$

Finally, we compensate for hour-angle-dependent reduction in the CHIME–Galt correlation amplitude due to the ~1,500-ns delay of the arrival of the Galt telescope signals at the correlator relative to the signals from the CHIME antennas. We evaluate this response at

the position of closest approach of the Crab nebula to the burst location in the CHIME beam using data collected 24 January 2019. In rough terms, we find that the primary beam at this location has 0.5% of the meridian response in the lower half of the band, falling to 0.1% of the meridian response in the top half of the band. Beyond this general trend, the primary-beam response across the band is dominated by spectral structure on ~30-MHz scales, owing to multiple reflections within the telescope.

SGR 1935+2154 is in the declination range that is seasonally covered by the Sun. An empirical beam model covering the full solar declination range was built using CHIME interferometric data from 2018 and 2019. To construct the model, we beamform to the location of the Sun using the purely north–south (same-cylinder) baselines. This average thus includes feed-to-feed variations in both amplitude and decoherence that are due to variations in phase. We expect these variations to be statistically representative, although not with the same feed weights as the FRB beamformer. The solar data are also analytically corrected for digital clipping that occurs owing to the limited bit depth of the correlator. Separate beam models are constructed for the east–west and north–south antenna polarizations, which are then summed. The flux of the Sun is cross-calibrated with the Crab nebula, when they share a common declination. Although the flux of the Sun is variable, the proximity in declination of SGR 1935+2154 to the Crab nebula, and that the data were collected near solar minimum, reduce the likelihood that the solar flux is varying greatly. We do not attempt to correct for the spatial extent of the Sun, which is ~0.5° in diameter and therefore resolved by the longest baselines. Averaged across the band, we roughly estimate that this effect accounts for a 20% reduction in the observed solar flux. However, because the baselines are in the north–south direction, the fraction of resolved flux should be nearly constant between the beam location of the burst and calibration with the Crab nebula. The resulting primary beam has qualitatively similar structure to that measured from holography, but an amplitude that is roughly a factor of two lower at the observed location of the burst (implying a higher intrinsic flux of the SGR 1935+2154 burst). This difference between solar and holography calibration methods is larger than expected and is taken as a systematic contribution to the flux measurement.

We further verify these beam-response measurements using beamformed data for the Crab nebula acquired through the FRB backend. This measurement is more direct than combining interferometric measurements of the primary beam with a model for the formed beams. However, the measurement is noisy because it suffers from source confusion; other sources contribute considerable flux when the Crab nebula is attenuated by the sub-per cent-level beam response. Baseline subtraction is also challenging because we cannot slew the sidelobe to an off-source location. Nonetheless, the Crab nebula is clearly detected even at hour HA = 22° and validates our beam measurements to a level of the order of 10%, in better agreement than the measurements obtained with holography and solar data.

We proceed with flux and fluence determination using measurements of the primary beam from both holography and solar data. Our quoted flux densities and fluences are the averages of those obtained with the two primary-beam models. As the beam responses from the three measurements agree only at the factor-of-two level, we conservatively ascribe a factor-of-two systematic error to both the flux density and fluence estimates to account for this disagreement. Further analysis and observations will be required to improve the far-sidelobe calibration accuracy.

For each beam in which SGR 1935+2154 was detected, we calculate beam-attenuated fluence spectra for both sub-bursts by integrating over the extent of each burst in the CHIME/FRB dynamic spectrum. We derived peak-flux spectra by multiplying the fluence spectra by the fluence-to-peak-flux ratio for each frequency channel calculated from the best-fit model of the intrinsic burst spectrum (described in the next section, 'Burst morphology and spectra'). Absolute flux scaling is derived from the real-time array calibration that is determined daily from bright-source transits and applied before beamforming (accounting for scaling factors inherent to the beamforming algorithm). In addition, we multiply our final flux-density values by a factor of 1.09 to account for the flux that is aliased outside the burst extent as a result of spectral leakage during the frequency channelization process.

We fitted the measured fluence and peak-flux spectral data to a model including the primary beam, formed beam and burst spectrum. We model the composite beam as the product of the measured primary beam and formed beams. Our primary-beam measurements are feed-averages of the complex primary beam (see equation (1)), and so our model accounts for reductions in the sensitivity of the synthesized beam that are due to beam phase variations, which, at this hour angle, is a ~20% effect at the bottom of the band and an effect of the order of unity at the top of the band. Beam phase variations also cause an increase in the formed-beam sensitivity at frequencies where they would have a null response in the absence of phase variations, and this effect is not accounted for. As such, in the fits we only include spectra for the four beams with the largest response, where the fits are dominated by frequencies of high formed-beam sensitivity. We model the intrinsic spectrum as a power law with a spectral running (see below). The model also includes two free parameters to shift the positions of the grid of formed beams relative to the source. This is necessary owing to a known systematic drift between the formed-beam model and the true position of the formed beams as a function of distance from the CHIME meridian, which is currently under investigation. The fit yields a position offset of 0.1°, and is nearly identical between fits to the first and second sub-bursts. We use least-squares with equal weighting to fit the spectra from the four beams to the data. For our reported fluences and fluxes, we average the best-fit spectral model over 400 to 800 MHz.

Burst morphology and spectra

We analysed the CHIME/FRB dynamic spectrum using a multi-component modelling scheme and least-squares algorithm described in previous works[6]. The model spectrum consists of two distinct components, assumed to be intrinsically Gaussian in temporal shape. Both of the model components have identical dispersion and scattering properties applied (that is, dedispersed to the same DM, and scatter-broadened by the same one-sided exponential pulse-broadening function). Each component has an independently determined arrival time, amplitude and spectral shape, and a temporal width that is corrected for broadening from single-tail scattering and dispersion smearing. The spectral energy distribution as a function of frequency, $I(f)$, is assumed to follow a weighted power-law form,

$$I(f) \propto (f/f_0)^{\gamma + r\,\ln(f/f_0)},$$

The spectral index (γ) and 'running' of the spectral index (r) are free parameters when modelling the dynamic spectrum, whereas the reference frequency (f_0) is held fixed to an arbitrary value. Moreover, the dispersion delay is $\Delta_{DM} = k\mathrm{DM}f^{-2}$, with $k = 4{,}149.377\ \mathrm{s\ pc^{-1}\ cm^3\ MHz^2}$, and the scattering timescale is assumed to be proportional to f^{-4}.

Unlike previous analyses, the two-component model used for parameter estimation was weighted by the frequency-dependent beam response in the direction of SGR 1935+2154 described in the preceding subsection. Such weighting accounts for spectral effects due to sidelobe detection, and thus allows for direct modelling of the 'intrinsic' (that is, beam-corrected) dynamic spectrum. Use of the beam-response model during the least-squares estimation of burst parameters is statistically preferred over models that do not explicitly account for the instrumental fringe pattern. No attempt was made to directly account for the faint 'ghost' leakage artefacts in the observed spectrum when fitting for the best-fit model, and will be the subject of future work.

The intrinsic and beam-attenuated models, as well as the observed dynamic spectrum and best-fit residuals (that is, differences between

the model and data), are shown in Extended Data Fig. 1. Remaining non-zero structure in the residuals probably reflects departures from the simplistic assumptions made for describing the spectral energy distribution.

Parameters describing burst morphology in the beam-weighted spectrum obtained from χ^2 minimization are presented in Table 1. We estimated a best-fit significance of the burst—defined as $S/N = \sqrt{\Delta\chi^2}$, where $\Delta\chi^2$ denotes the difference between the best-fit χ^2 and the same statistic for a model with zero burst amplitude—to be $S/N = 264$. This S/N is considerably larger than the value obtained when not directly modelling for frequency-dependent scattering of the burst—$S/N = 245$ in this case—which indicates that the model with single-tailed scattering is statistically preferred ($P \approx 10^{-16}$) when using the F-test statistic in comparing nested models.

Algonquin Park 10-m radio telescope observations

The Algonquin Radio Observatory (ARO) hosts a stationary 10-m single-dish telescope in Algonquin Provincial Park, Ontario, Canada. The telescope uses a cloverleaf feed identical to that on CHIME[56], using ICEboard as a digital backend[57], with a frequency range of 400–800 MHz using the same native 1,024-bin channelization as CHIME. The system is continuously recording baseband data to a rolling 24.5-h disk buffer and was pointed at (RA, dec.) = (21 h 12 min, 22°) at the time of the radio burst from SGR 1935+2154. The baseband data were manually saved after the CHIME event, which in the future should occur automatically.

Owing to the pointing and localization from the CHIME detection, the event was detected in a far sidelobe of the ARO beam. The burst was identified in the data with the CHIME-measured timing. Each linear polarization was coherently dedispersed with DM = 332.80 pc cm^{-3}, and the Stokes Q, U and V parameters were formed by subtracting the off-pulse component. The off-pulse per-channel root-mean-square values are used as weights for the polarization analysis[8].

The first burst (B1) is detected in both polarizations. We use RM synthesis to measure its RM from the Stokes Q and U parameters, after correcting instrumental leakages. The resulting Faraday spectrum is shown in Extended Data Fig. 2a, contributing to final RM = 116 rad m^{-2} (see below).

The second burst (B2) is only visible in one linear polarization in the ARO data (which we label Y), owing to frequency variations in the polarized sidelobe response. To account for this, we infer the RM through the flux in the polarized flux YY^*, which is related to the Q and I Stokes parameters by $YY^* = (I + Q)/2$. We perform RM synthesis[58,59] on YY^*. We identify a peak in the amplitude of the Faraday spectra at RM ≈ 116 rad m^{-2} (Extended Data Fig. 2b). The RM measured in this way will be free from the influence of U–V leakage and have different systematics compared to the measurement using Q and U.

We verify this method using two bright giant pulses from the Crab pulsar detected with the same instrument. We are able to recover identical values of RM and polarization angle (PA) difference from the single linear polarization as those obtained from combining Stokes Q and U, although with half the signal. Moreover, we compare the Faraday spectra from YY^* only with the traditional one from combining Q and U for B1. The offset between the measured RM and PA from those approaches are 0.7 rad m^{-2} and 1.6°, which are well within the uncertainties. The Crab nebula data are also used to determine the sign of RM[60].

We cross correlate the Q–U Faraday spectra $F_{\rm B1}$ from the first burst with the YY^* Faraday spectra $F_{\rm B2}$ from the second burst $F_{\rm cross} = \sqrt{F_{\rm B1}F^*_{\rm B2}}$. Assuming no RM changes between the two bursts, separated by only 29 ms, the phase of the cross spectrum corresponds to the PA difference between the two bursts. A maximum cross-correlation signal appears at RM = 116 ± 2 ($\sigma_{\rm measurement}$) ± 5 ($\sigma_{\rm systematic}$) rad m^{-2}, with a PA difference of 5° ± 10° between the bursts at the peak. As shown in Extended Data Fig. 2c, near the peak, the real part of the cross spectrum dominates the amplitude, indicating that the PA difference is small, consistent with zero. The systematic uncertainty $\sigma_{\rm systematic}$ is estimated from the change of inferred RM owing to different Stokes U–V leakage models, that arise from a combination of sidelobe phases and differential cable delays, as well as uncertainties of the underlying spectral shapes.

Although CHIME has recorded only intensity data, the oscillations of Stokes Q due to Faraday rotation can leak into the summed intensity through the different responses of the two linear polarization feeds in the far sidelobe. Consequently, we can estimate the RM and PA differences using a similar procedure to the baseband analysis. We see a signal near RM ≈ 116 rad m^{-2} for both bursts. The cross spectrum is shown in Extended Data Fig. 2d, with a peak at 115.3 rad m^{-2}. The measured PA difference at the peak of the cross spectrum is 4° ± 10°, consistent with the result from the ARO 10-m radio telescope.

Extended Data Fig. 3 shows the model of fitted PA and RM against data for B1, where the characteristic signal of Faraday rotation is identified. The measured RM is similar to that reported by FAST (RM = 112.3 rad m^{-2}) for a different burst from the same source[19]. Taken together, these factors indicate that the ARO-measured RM is robust in spite of the unknown systematics. Robust linear and fractional polarization measurements await calibration with a beam model that has been validated with bright sidelobe events of known sources.

CHIME/FRB non-detections of November 2019 high-energy bursts from SGR 1935+2154

SGR 1935+2154 is in an extended active phase that commenced in October 2019, and which has included many dozens of X-ray and γ-ray bursts. Four high-energy bursts occurred in November 2019 when the source was closer to CHIME's meridian than for the 28 April 2020 burst. Specifically, bursts on 4 November 2019 at 01:20:24 seen by the Fermi Gamma-ray Burst Monitor[28], and 01:54:37 seen by the Swift Burst Alert Telescope (BAT)[29], as well as on 5 November 2019 at 00:08:58 and 01:36:25, both seen by Swift/BAT[29,30], were, respectively, at CHIME hour angles 9.5°, 18.1°, −7.4° and 14.5° when they occurred. All four occurred during nominal CHIME/FRB operations. No radio burst was detected by our automated pipeline at any of the four high-energy burst epochs. (We also ran a custom implementation of the clustering algorithm DBSCAN[61] tailored to the CHIME/FRB pipeline to identify any other events from this source at any epoch, including in the sidelobes, but found no detections.) Using our current best models to account for CHIME's primary-beam response, the formed-beam response, and system sensitivity (corroborated using techniques analogous to those described above), and scaling the measured fluences for three detected FRBs at nearly the same declination as SGR 1935+2154 using their detection signal-to-noise ratios and the CHIME/FRB detection threshold of 10, we determine a conservative upper limit on radio burst flux density in the 400–800 MHz range of <1.7 kJy, <4.6 kJy, <1.2 kJy and <3.0 kJy for the four events, respectively, within an approximately 3σ confidence interval, though we caution that the challenges of working in the far sidelobe make a precise confidence interval difficult to calculate. Thus, radio bursts at the epochs of these high-energy events from SGR 1935+2154 had 400–800-MHz radio flux-density factors at least 30–120 times lower than the 28 April 2020 event.

For the two bursts on 5 November 2019, we determine the X-ray flux from the processed online public BAT data products using version 12.10.1f of HEASARC's XSPEC program[62]. Although the high-energy fluxes for the bursts on 4 November 2019 will be considered in future work, we note that the Swift/BAT burst at 01:54:37 on 4 November is much weaker than the two Swift/BAT bursts on 5 November. For the burst at 00:08:58, we find the data are well modelled using two blackbody components. Fixing the equivalent neutral hydrogen absorption column[14] $N_{\rm H}$ to 1.6×10^{22} cm^{-2}, we find a reduced χ^2 of 1.05 for this model. The 20–200-keV flux is then $6.6^{+0.4}_{-0.4} \times 10^{-7}$ erg cm^2 s^{-1}. For the 5 November burst at 01:36:25, we follow a similar procedure and use a double blackbody model to find reduced $\chi^2 = 0.79$. The 20–200-keV flux is then $8.4^{+0.2}_{-0.3} \times 10^{-7}$ erg cm^2 s^{-1}. Thus, both of the 5 November 2019 bursts had X-ray fluxes 14 and 11 times smaller, respectively, than the reported

Konus-Wind 20–200-keV high-energy flux[23] on 28 April 2020 ($(9.1 \pm 2.6) \times 10^{-6}$ erg cm^2 s^{-1}), in contrast to being, respectively, more than 120 and 50 times smaller in the CHIME band. This shows the radio-to-X-ray flux ratios for these 2019 events were at least 9 and 4 times smaller, respectively, than for the 28 April 2020 event.

Comparison between volumetric rates of magnetar flares and FRBs

We estimate the total number of active magnetars in the CHIME-visible volume by scaling the total star-formation rate in nearby galaxies to that of the Milky Way. From the complete sample of galaxies[63] within 11 Mpc, the distance to which the 28 April SGR 1935+2154 burst, at its best-estimated 400–800-MHz flux density, would have been seen by CHIME/FRB, we selected 15 galaxies in the CHIME field of view (declination >−10°) that had high star-formation rates and large CHIME exposure (Extended Data Table 1). The total star-formation rate in these galaxies is approximately $36 M_\odot$ yr^{-1} ($M_\odot$, mass of the Sun), based on Hα intensity estimates and total far-ultraviolet luminosity (where Hα estimates were not available) and far-infrared luminosity[64] for the M82 galaxy ($\gtrsim 10 M_\odot$ yr^{-1}). Given the star-formation rate in the Milky Way (approximately $1 M_\odot$ yr^{-1}) and the population of around 30 active magnetars[2], we estimate about 10^3 active magnetars exist in this volume.

During CHIME/FRB's operations since September 2018, we have not observed an FRB above $S/N = 9$ from any of these galaxies. Given this non-detection, we can set an upper limit on the rate of SGR 1935+2154-like bursts from any magnetar in this range. We estimated the exposure time of CHIME/FRB to these galaxies and calculated the sum of the exposure times of all the galaxies weighted by their star-formation rate (and hence the number of active magnetars). We estimate that the total exposure of CHIME/FRB was 6×10^4 magnetar-hours.

The 95% confidence upper limit[65] on the rate of SGR 1935+2154-like bursts with energy $E > 10^{34}$ erg per magnetar is $R_B(E > 10^{34}\ \text{erg}) < 5 \times 10^{-5}\ \text{hr}^{-1} \approx 0.4\ \text{yr}^{-1}$.

The lower limit on the rate of magnetar bursts in the galaxy comes from the single detection of a burst from SGR 1935+2154. Ten of the 30 Galactic magnetars pass over the CHIME primary beam. A bright burst similar to the one from SGR 1935+2154 would be detectable by CHIME if the source was above the horizon. With an on-sky time of one-and-a-half years since September 2018, we can estimate a 95% lower limit[65] on the rate to be $R_B(E > 10^{34}\ \text{erg}) > 7 \times 10^{-3}\ \text{yr}^{-1}$.

The ASKAP telescope searched for bursts from the Virgo cluster at 16.5 Mpc with a 300-hour-long observation[46] with a 10σ sensitivity of approximately 30 Jy ms. At a distance of the Virgo cluster and with the observing bandwidth of 336 MHz, this fluence threshold corresponds to a burst energy of ~10^{36} erg. The star-formation rate in the Virgo cluster is estimated to be $776 M_\odot$ yr^{-1}, corresponding to about 2.3×10^4 SGR 1935+2154-like magnetars. Thus, the upper limit on the rate of magnetar bursts is $R_B(E > 10^{36}\ \text{erg}) < 4 \times 10^{-7}\ \text{hr}^{-1} \approx 4 \times 10^{-3}\ \text{yr}^{-1}$.

Data availability

The data used in this publication are available at https://chime-frb-open-data.github.io and in the repository at https://doi.org/10.11570/20.0006.

Code availability

The code used in this publication is available at https://chime-frb-open-data.github.io.

51. Ng, C. et al. CHIME FRB: an application of FFT beamforming for a radio telescope. In *Proc. XXXII General Assembly and Scientific Symp. Intl Union of Radio Science (URSI GASS)* J33-2 (2017).
52. Masui, K. W. et al. Algorithms for FFT beamforming radio interferometers. *Astrophys. J.* **879**, 16 (2019).
53. Foreman-Mackey, D., Hogg, D. W., Lang, D. & Goodman, J. emcee: the MCMC hammer. *Publ. Astron. Soc. Pacif.* **125**, 306 (2013).
54. Newburgh, L. B. et al. Calibrating CHIME: a new radio interferometer to probe dark energy. *Proc. SPIE* **9145**, 91454V (2014).
55. Berger, P. et al. Holographic beam mapping of the CHIME pathfinder array. In *Ground-based and Airborne Telescopes VI* (eds Hall, H. J., Gilmozzi, R. & Marshall, H. K.) 99060D (SPIE, 2016).
56. Bandura, K. et al. Canadian Hydrogen Intensity Mapping Experiment (CHIME) pathfinder. In *Ground-based and Airborne Telescopes V* (eds Stepp, L. M., Gilmozzi, R. & Hall, H. J.) 914522 (SPIE, 2014).
57. Bandura, K. et al. ICE: a scalable, low-cost FPGA-based telescope signal processing and networking system. *J. Astron. Instrum.* **5**, 1641005 (2016).
58. Burn, B. J. On the depolarization of discrete radio sources by Faraday dispersion. *Mon. Not. R. Astron. Soc.* **133**, 67–83 (1966).
59. Brentjens, M. A. & de Bruyn, A. G. Faraday rotation measure synthesis. *Astron. Astrophys.* **441**, 1217–1228 (2005).
60. Sobey, C. et al. Low-frequency Faraday rotation measures towards pulsars using LOFAR: probing the 3D Galactic halo magnetic field. *Mon. Not. R. Astron. Soc.* **484**, 3646–3664 (2019).
61. Ester, M., Kriegel, H.-P., Sander, J. & Xu, X. A density-based algorithm for discovering clusters in large spatial databases with noise. In *Proc. Second Intl Conf. Knowledge Discovery and Data Mining, KDD'96* (eds Simoudis, E., Han, J. & Fayyad, U.) 226–231 (AAAI, 1996).
62. Arnaud, K. A. Xspec: the first ten years. In *Astronomical Data Analysis Software and Systems V* (eds Jacoby, G. & Barnes, J.) 17 (ASP, 1996).
63. Karachentsev, I. D. & Kaisina, E. I. Star formation properties in the local volume galaxies via Hα and far-ultraviolet fluxes. *Astron. J.* **146**, 46 (2013).
64. Jarrett, T. H. et al. The WISE Extended Source Catalog (WXSC). I. The 100 largest galaxies. Astrophys. *J. Suppl. Ser.* **245**, 25 (2019).
65. Gehrels, N. Confidence limits for small numbers of events in astrophysical data. *Astrophys. J.* **303**, 336–346 (1986).

Acknowledgements We thank the Dominion Radio Astrophysical Observatory, operated by the National Research Council Canada, for hospitality and expertise. The CHIME/FRB Project is funded by a grant from the Canada Foundation for Innovation (CFI) 2015 Innovation Fund (Project 33213), as well as by the provinces of British Columbia and Quebec, and by the Dunlap Institute for Astronomy and Astrophysics at the University of Toronto. Additional support was provided by the Canadian Institute for Advanced Research (CIFAR), McGill University and the McGill Space Institute via the Trottier Family Foundation, and the University of British Columbia. CHIME is funded by a grant from the CFI Leading Edge Fund (2012) (project 31170) and by contributions from the provinces of British Columbia, Quebec and Ontario. The Dunlap Institute is funded by an endowment established by the David Dunlap family and the University of Toronto. Research at Perimeter Institute is supported by the Government of Canada through Industry Canada and by the Province of Ontario through the Ministry of Research and Innovation. The National Radio Astronomy Observatory is a facility of the National Science Foundation operated under cooperative agreement by Associated Universities, Inc. M.B. is supported by a Fonds de Recherche Nature et Technologie Québec (FRQNT) Doctoral Research Award. P.C. is supported by an FRQNT Doctoral Research Award. M.D. is supported by a Killam Fellowship and receives support from an NSERC Discovery Grant, CIFAR, and from the FRQNT Centre de Recherche en Astrophysique du Québec (CRAQ). B.M.G. acknowledges the support of NSERC through grant RGPIN-2015-05948, and of the Canada Research Chairs programme. J.W.K. is supported by NSF award 1458952. V.M.K. holds the Lorne Trottier Chair in Astrophysics and Cosmology, a Distinguished James McGill Professorship and receives support from an NSERC Discovery Grant (RGPIN 228738-13) and a Gerhard Herzberg Award, from an R. Howard Webster Foundation Fellowship from CIFAR, and from the FRQNT CRAQ. D.M. is a Banting Postdoctoral Fellow. S.M.R. is a CIFAR Fellow and is supported by the NSF Physics Frontiers Center, award 1430284. U.-L.P. receives support from Ontario Research Fund–Research Excellence (ORF-RE) programme, CFI, the Simons Foundation and the Alexander von Humboldt Foundation. U.-L.P. acknowledges support from NSERC (grant RGPIN-2019-067 and CRD 523638-201). Z.P. is supported by a Schulich Graduate Fellowship from McGill University. P.S. is a Dunlap Fellow and an NSERC Postdoctoral Fellow. FRB research at UBC is supported by an NSERC Discovery Grant and by CIFAR.

Author contributions All authors from the CHIME/FRB Collaboration had either leadership or significant supporting roles in one or more of: the management, development and construction of the CHIME telescope, the CHIME/FRB instrument and the CHIME/FRB software data pipeline, the commissioning and operations of the CHIME/FRB instrument, the data analysis and preparation of this manuscript. All authors from the CHIME Collaboration had either leadership or significant supporting roles in the management, development and construction of the CHIME telescope.

Competing interests The authors declare no competing interests.

Additional information

Supplementary information is available for this paper at https://doi.org/10.1038/s41586-020-2863-y.

Correspondence and requests for materials should be addressed to P.S.

Peer review information *Nature* thanks Evan Keane and Amanda Weltman for their contribution to the peer review of this work. Peer reviewer reports are available.

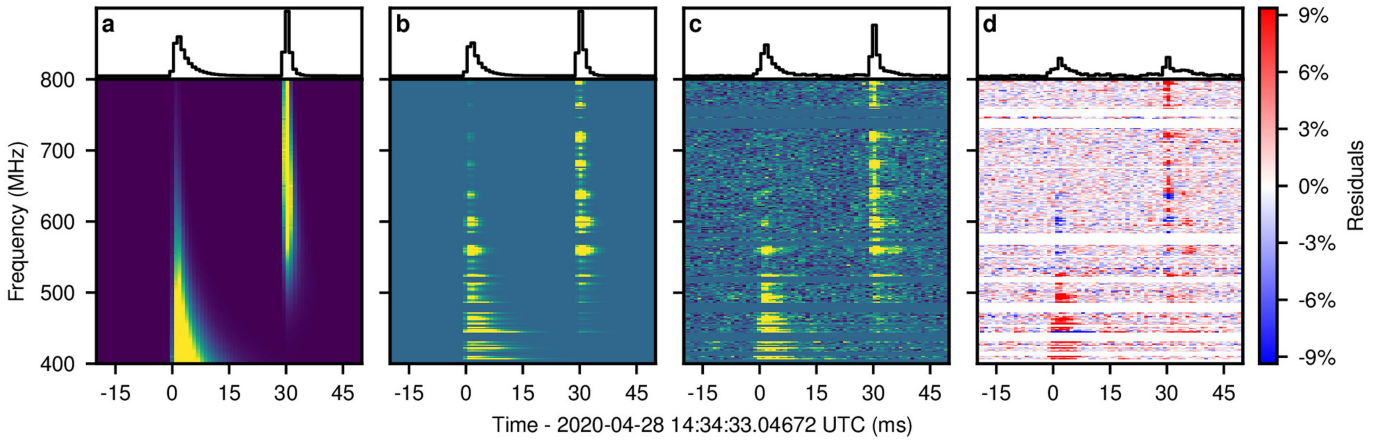

Extended Data Fig. 1 | Burst fitting. a–**d**, Dynamic spectra and band-averaged time series (referenced to the geocentre) of fitted burst models (**a**), beam-attenuated burst models (**b**), burst data as in Fig. 1 (**c**) and fit residuals (**d**). Dynamic spectra are displayed at 0.98304-ms and 1.5625-MHz resolution, with intensity values capped at the 1st and 99th percentiles, except in **d** where values are capped at $\pm 3\sigma$ around 0. The time series of **b**–**d** have the same scaling. The beam attenuation of the maxima in the model dynamic spectra is about 1,700×.

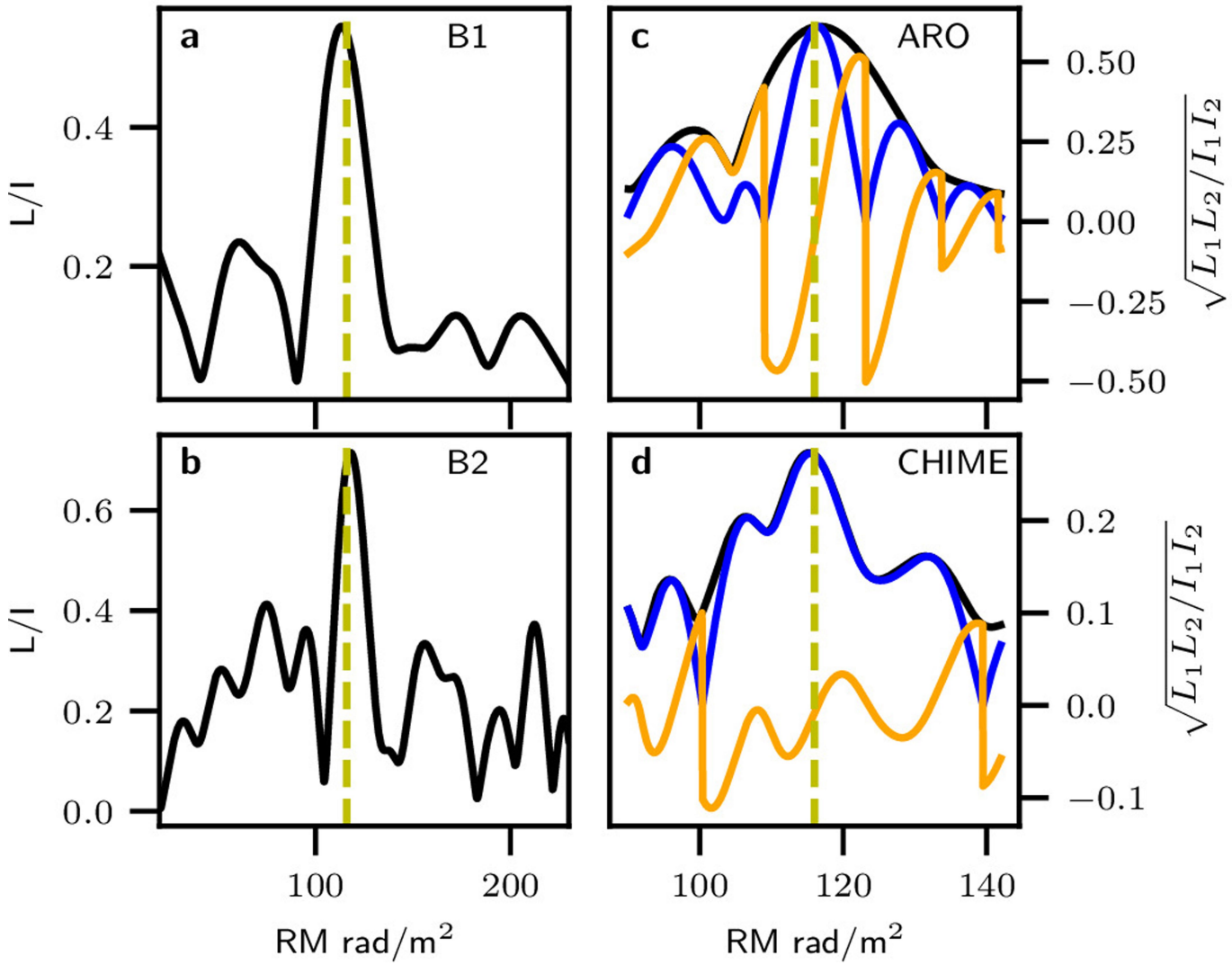

Extended Data Fig. 2 | Polarized intensity Faraday spectra for the two bursts. a, The Faraday spectrum F_{B1} for the first sub-burst from Stokes Q and U after correcting for a leakage between Stokes U and V. **b**, Faraday spectrum F^*_{B2} for the second sub-burst from a single polarized flux of the ARO 10-m dish. **c**, The cross spectrum $F_{cross} = \sqrt{F_{B1}F^*_{B2}}$ from the ARO 10-m dish, magnified near the peak. **d**, The cross spectrum from CHIME intensity data. The oscillations of the Stokes Q from Faraday rotation have leaked to the summed intensity, owing to the different response of the two linear receivers in the far sidelobe. The black lines show the amplitude of the spectra; the blue and orange lines are the real and imaginary parts of the spectra, respectively. The phase of the cross spectrum corresponds to the PA difference between the two bursts. When the real part approaches the amplitude, the two bursts have the same PA. The yellow dashed vertical line is drawn at RM = 116 rad m^{-2}. L is the linear polarization, I is the total intensity and their indices refer to the first and second bursts.

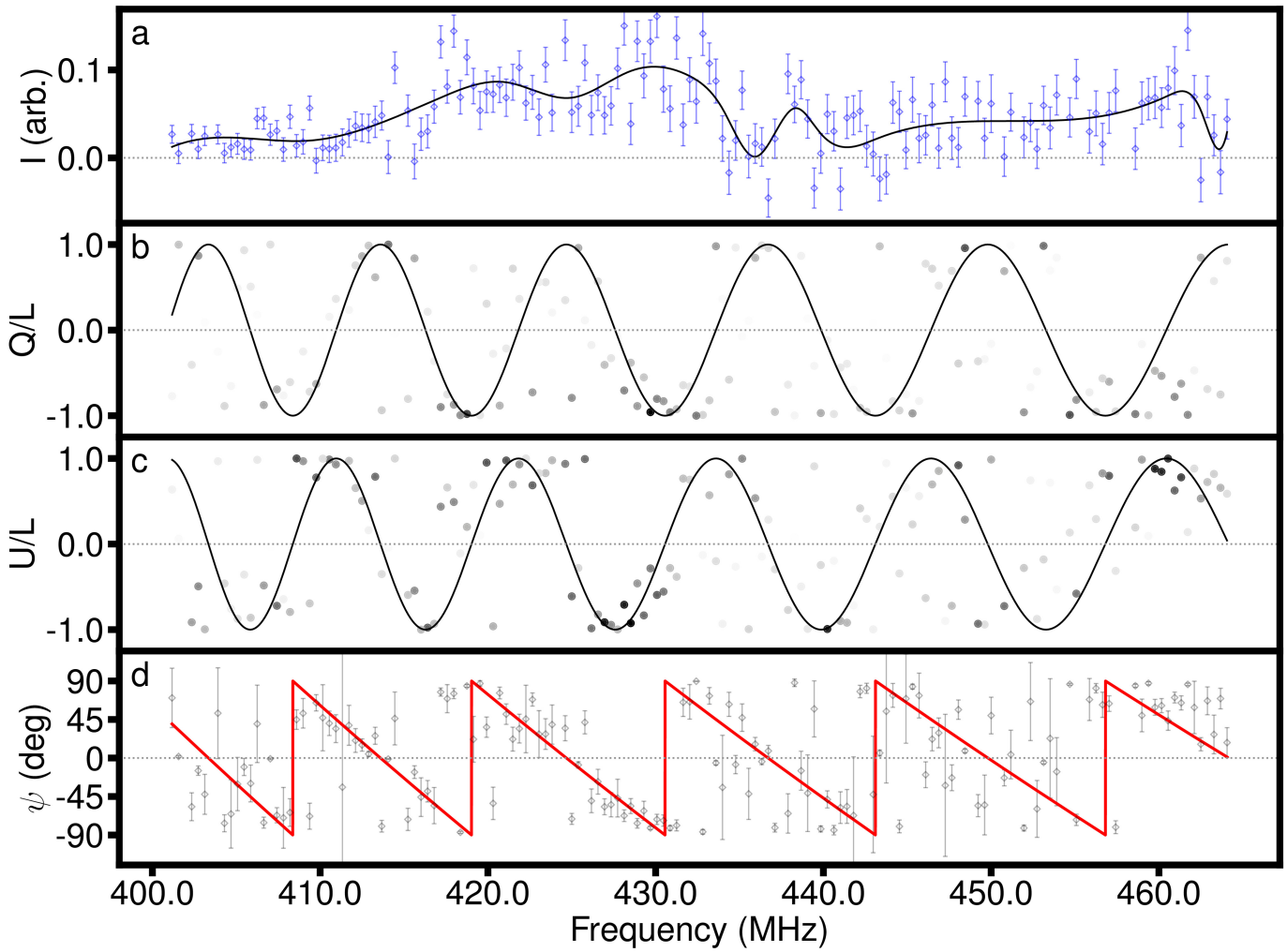

Extended Data Fig. 3 | The polarization spectra for the first observed burst from the ARO 10-m telescope. a–d, The spectrum of the first burst in the Stokes *I* parameter and its cubic spline-smoothed version (black line) (**a**), the Stokes *Q* parameter divided by the total linear polarization, *L* (**b**), the Stokes *U* parameter divided by the total linear polarization (**c**), and the uncalibrated polarization angle, ψ (**d**). The frequency channels with greater polarized intensity are indicated with darker points. The best-fit model of the Faraday rotation modulation with an RM of 116 rad m^{-2} is indicated by the black lines in **b** and **c**. The best-fit model of the uncalibrated polarization angle is indicated with the solid red line in **d**. Error bars are 1σ.

Extended Data Table 1 | Nearby star-forming galaxies

Name	RA (deg)	Dec (deg)	Distance (Mpc)	SFR ($\mathrm{M_\odot\,yr^{-1}}$)	Exposure* (hrs)
NGC 4559	188.99	27.96	7.4	1.1	35
NGC 4490	187.65	41.64	6.9	0.79	51
NGC 1569	67.70	64.85	3.2	0.78	58
UGCA 127	95.23	-8.50	10.0	1.3	40
NGC 4258	184.74	47.30	7.7	2.9	21
NGC 3556	167.88	55.67	9.6	0.91	68
NGC 5194	202.47	47.23	7.6	3.0	21
M81	148.89	69.07	3.7	0.98	66
NGC 2903	143.04	21.50	9.2	1.9	38
NGC 3521	166.45	-0.04	8.5	3.2	23
NGC 3627	170.06	12.99	8.5	2.3	32
NGC 5055	198.96	42.03	9.0	1.6	50
M101	210.80	54.35	6.95	3.3	40
NGC 6946	308.71	60.15	7.7	2.5	74
M82	148.97	69.68	3.6	10	94

*Exposure in the full-width at half maximum of CHIME beams.
SFR, star-formation rate.